

Piezo-Phototronic UV/Visible Photosensing with Optical-Fiber–Nanowire Hybridized Structures

Zhaona Wang, Ruomeng Yu, Caofeng Pan, Ying Liu, Yong Ding, and Zhong Lin Wang*

Optical fiber (OF) and OF-based systems are of significant importance for optical-communication systems, smart sensor networks,^[1] compact optical measurement systems,^[2] and many more applications,^[3] because of the low transportation losses and high bandwidth for electromagnetic wave propagation. Generally, a coupler is necessary between the optical fiber and the photodetector (PD) for the conversion of optical signals to electrical signals. The energy losses through this coupling process have been an inevitable obstacle for improving the efficiency, lowering the costs, and enhancing the quality of information communication.^[4,5] Therefore, newly designed PDs with the capability of being integrated with standard optical fibers in an energy-efficient manner may become necessary. Semiconducting nanowire arrays, which are well known for their unique structural characteristics and versatile physical properties,^[6–9] serve as building blocks for a variety of optoelectronic devices,^[10] and in particular for ultra-sensitive and rapid-response PDs.^[11–17] However, most reported PDs are fabricated based on the conventional plane configurations, which require a coupler to connect with optical fibers, which results in energy losses.

In this work, we demonstrate the implementation of direct integration between an optical communications system and PDs by designing and fabricating UV/visible photosensing devices that contain an optical-fiber–nanowire hybridized structure (Figure 1a). ZnO/CdS nanowire (NW) heterojunctions are synthesized coaxially around an optical fiber (OF) to allow ultraviolet and visible light detection. The PD operates in two modes: axial and off-axial illumination mode. Upon straining, piezo-polarization charges present at the ZnO/CdS heterojunction interface effectively tune/control the charge transport across the interface/junction and modulate the optoelectronic processes of local carriers, such as generation, separation, diffusion, and recombination. This phenomenon is called the piezo-phototronic effect,^[18] a three-way coupling of piezoelectric

polarization, semiconductor and photon excitation in wurtzite-structured piezoelectric semiconductors, which have been used to greatly enhance the photoresponsivity of PDs^[11,19] and the emission efficiency of LEDs.^[8,20] The performance of PDs has been enhanced/optimized by up to 718% in sensitivity and 2067% in photoresponsivity.

The structure of an OF–NW hybridized UV/visible PD is schematically illustrated in Figure 1b. A detailed discussion of the fabrication process is provided in the Experimental Section. The top-view and side-view scanning electron microscopy (SEM) images shown in Figure 1c and d confirm the PD configuration, and indicate that the OF core is uniformly and compactly covered by a ZnO NW array with diameters of 150–250 nm and lengths of 3–4 μm (Figure 1c); the layer of CdS NWs on top had a thickness of about 1 μm (Figure 1d). ZnO NW arrays are grown coaxially along the *c*-axis in an outward radial direction of the OF, as indicated by the select-area electron diffraction (SAED) pattern from a single ZnO NW (Figure 1e). The existence of a heterojunction interface between ZnO and CdS NWs was verified by measuring energy dispersive X-ray (EDX) spectra (Figure 1f) of a single nanowire that was collected from the corresponding areas marked in Figure 1d2 by red and blue circles. Only ZnO is present at the inner layer (blue circle), whereas both ZnO and CdS are observed at the outer layer (red circle), which is where the heterojunction is formed.

External strain was applied to the OF–NW hybridized PD by bending one end of the device with a 3D mechanical stage (movement resolution $\approx 10 \mu\text{m}$), while fixing the other end on a manipulation holder. If we consider the symmetric configuration of this device, bending the device upwards (or downwards) in a concave (or convex) fashion, as shown in Figure 2a, results in a compressive strain along the longitudinal direction of the OF that induces a tensile strain along the *c*-axis of the ZnO NWs at the top (or bottom) side of the OF, while no strain is experienced by ZnO NWs that are distributed at the bottom (or top) side of the OF due to the spacing between loosely assembled NWs in the local region (Figure 1c).^[21] Finite-element analysis was conducted to simulate the strain/piezoelectric potential distributions within the ZnO NWs arrays upon straining as shown in Figures 2b and c, based on a 2D physical model that uses the real dimensions of the OF–NW hybridized structure as parameters (see Supporting Information). When bending the OF upwards concavely, the simulation results clearly confirm the strain distribution analysis presented above, i.e., that NWs nearest to the OF at the top side are under tensile strain, while the NWs at the bottom are strain-free (Figure 2b). The piezopotential distributions are also illustrated in color codes by knowing the sign of externally applied strain (tensile strain on the top-side ZnO NWs along its *c*-axis) as well as the crystalline orientation of the ZnO NWs (*c*-axis pointing outwards along

Dr. Z. N. Wang, R. M. Yu, Dr. Y. Liu,
Dr. Y. Ding, Prof. Z. L. Wang
School of Materials Science and Engineering
Georgia Institute of Technology
Atlanta, GA 30332-0245, USA
E-mail: zhong.wang@mse.gatech.edu

Dr. Z. N. Wang
Department of Physics
Beijing Normal University
Beijing, China 100875

Prof. C. F. Pan, Prof. Z. L. Wang
Beijing Institute of Nanoenergy and Nanosystems
Chinese Academy of Sciences
Beijing, China 100083

DOI: 10.1002/adma.201405274



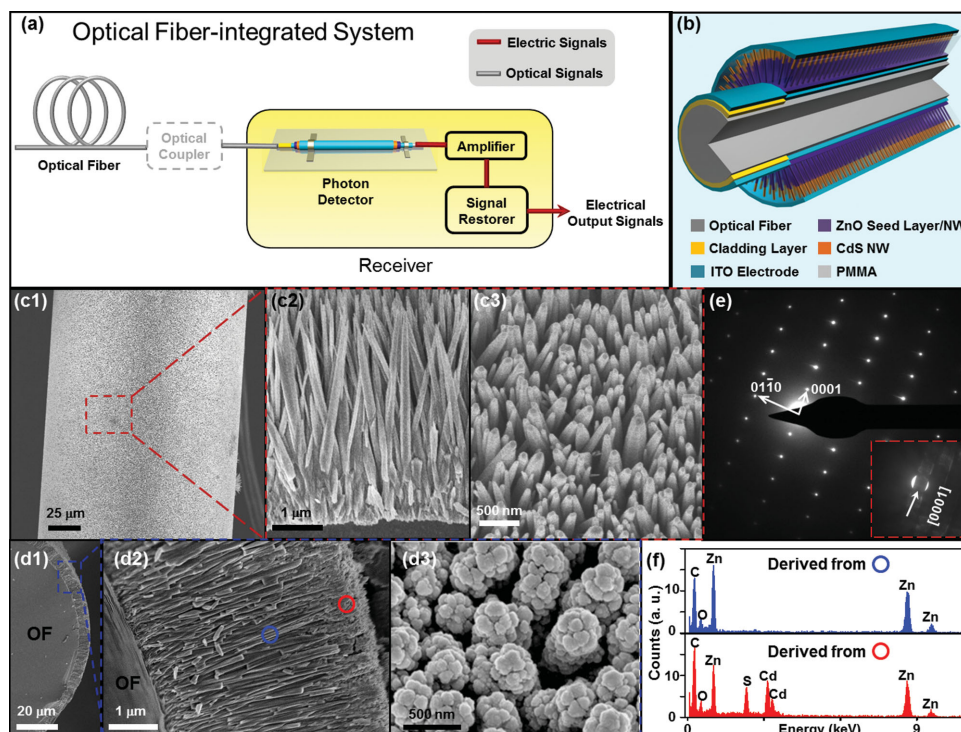


Figure 1. Structure and characterization of OF–NW hybridized UV/visible PDs. a) Schematic illustration of direct integration in an optical communications system in a coupler-free manner. b) Schematic demonstration of the structure of an OF–NW hybridized UV/visible PD. c, d) SEM images of a NW array synthesized coaxially around the OF. The enlarged side view and top view, before (c2, c3) and after formation of the ZnO/CdS heterojunctions (d2, d3) are shown. e) The corresponding select area electron diffraction (SAED) pattern of the ZnO NWs. f) Energy dispersive X-ray (EDX) spectra of single NWs collected from corresponding areas marked by the blue and red circles shown in (d2).

the radial direction of the OF).^[18,22] As shown in Figure 2c, the positive piezo-potential distributes along the ZnO NWs on the top side due to tensile strains, and no obvious potential was observed for the strain-free ZnO NWs at the bottom side. The values shown in Figure 2d correspond to the longitudinal strain along the OF^[23] with the tensile strain being defined as positive and the compressive strain as negative.

The influence of strain on the carrier transportation at the ZnO/CdS interface can be understood from the band diagram. An energy barrier is formed at the ZnO/CdS heterojunction interface (Figure 2e) due to the shift of the ZnO conduction band^[24] upward by eV_{bias} when ZnO NWs are reversely biased, as shown in the inset of Figure 2d. When applying an external strain, positive piezo-polarization charges are induced at the heterojunction interface, which effectively reduce the barrier height by lowering both the conduction and valence band of the ZnO NWs (Figure 2f). Dominated by the reversely biased barrier height, the electronic transport process is therefore significantly facilitated because local charge carriers pass through the heterojunction interface more easily. The higher the externally applied strain, the lower the barrier height, and thus a higher output current is observed, as can be seen from the I – V characteristics in Figure 2d. The inset of Figure 2d indicates a linear increase of the output current from 47 nA (strain free) to more than 331 nA (–0.86% strain) when the top electrode (CdS NWs) is biased at 2 V. Upon light illumination, the separation process of light-generated electron–hole pairs in the vicinity of the heterojunction interface is profoundly promoted by a lowered

barrier height owing to the presence of strain-induced positive piezo-polarization charges. This is the fundamental principle of a piezo-phototronic-effect enhanced/optimized performance of OF–NW hybridized UV/visible PDs.

Considering the absorption spectra of the ZnO NW array (Figure S1a, Supporting Information) and the ZnO/CdS heterostructure (Figure S1b), UV/visible detection was first investigated by applying incident light signals (325 nm laser as UV source, 532 nm laser as visible source) in two different manners, as schematically shown in Figure 3a and d. A 325 nm laser beam is focused at the cladding-layer-covered end of the OF (Figure 3a) as UV stimulus for the axial illumination mode. Higher light absorbance and detection sensitivity are expected for a PD in this mode of operation, because of the total internal reflection and multi-scattering within the OF. By varying the power densities of the incident light, a series of I – V characteristics can be measured. These are summarized in Figure 3b, and show a good photoresponse for the output current, which increases logarithmic-linearly from 41.4 nA (dark) to 158.8 nA ($9.5 \times 10^{-5} \text{ W cm}^{-2}$) (inset of Figure 3b and Figure S2a in the Supporting Information), when the top electrode (CdS NWs) is biased at 2 V. A laser beam of 532 nm was shined from the outside onto the surface of the PDs for visible detection in the off-axial illumination mode. Although the construction of these PDs merely allows one side of the NWs to be under direct illumination, most NWs can still interact with the incident light, when both transmitting and scattering of the beam by the transparent OF core is considered, and which cannot be

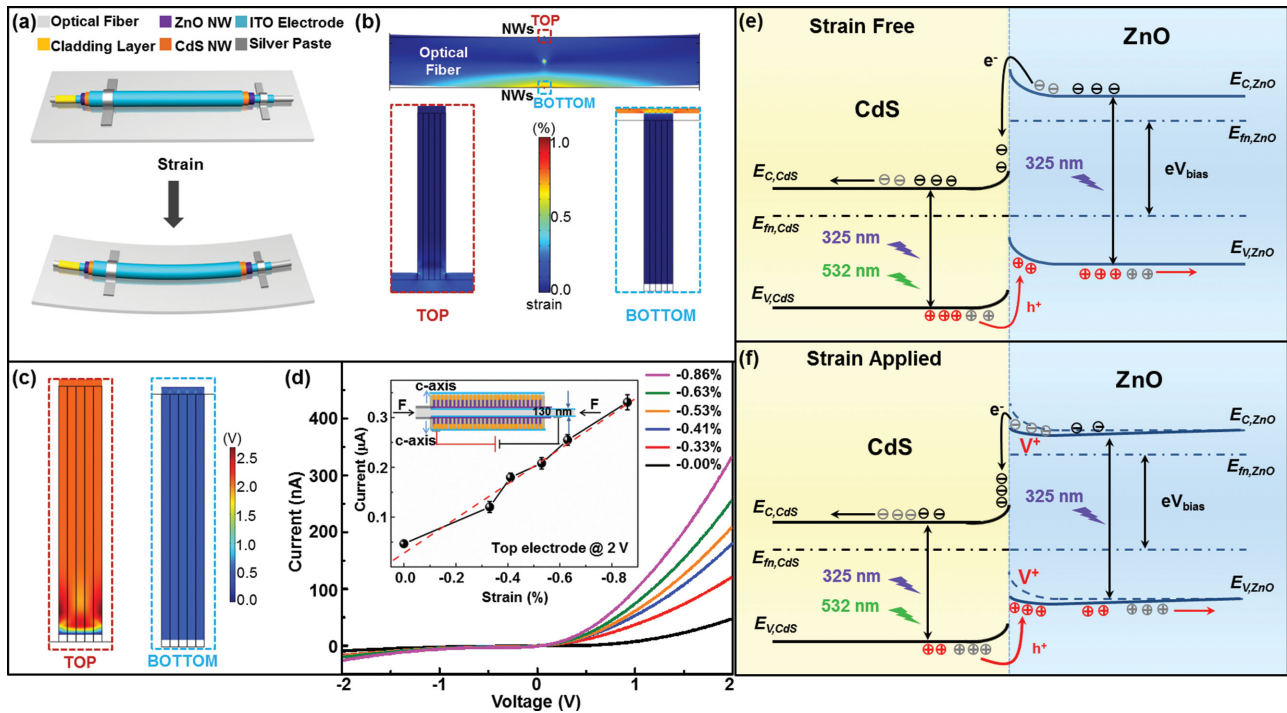


Figure 2. Piezo-phototronics and the working mechanism of OF–NW hybridized PDs. a) 3D schematic demonstration of OF–NW hybridized PDs without (top) and with strain (bottom). b) Simulation results of strain distributions of OF–NW hybridized PDs by the finite-element analysis method when bending the optical fiber concave up with a displacement of 10 μm . The physical model is based on the dimensions of real devices. Enlarged strain distribution within ZnO NWs for both the top (in the red square) and bottom side (in the blue square) of the OF are presented. c) Simulation results of piezoelectric potential distribution within the ZnO NW array on the top (in the red square) and bottom side (in the blue square) of the OF. A positive piezo-potential is produced within the top side ZnO NWs. d) I – V characteristics of an OF–NW hybridized dual-mode PD under different compressive strains by applying a triangular wave across the device, no light illumination involved. The inset shows a schematic experiment set-up and an I –strain curve when the top-electrode is biased at 2 V. e, f) Schematic band diagrams of ZnO/CdS heterojunctions without (e) and with external strain (f) applied to illustrate the working mechanism of OF–NW hybridized dual-mode PDs.

obtained from a traditional substrate such as carbon fiber.^[16] A similar optoelectronic behavior is observed for visible detection under off-axial illumination mode (Figure 3e), with the output current increasing logarithmic-linearly (inset of Figure 3e and Figure S2b) from 630 nA (dark) to 1594 nA ($9.5 \times 10^{-4} \text{ W cm}^{-2}$), when the top electrode (CdS NWs) is biased at 2 V.

The response time of the OF–NW hybridized PDs was carefully studied; the results are presented in Figure 3c and f for both UV and visible detection. The UV response presented in Figure 3c was obtained under 325 nm axial illumination with a power density of $5.9 \times 10^{-6} \text{ W cm}^{-2}$ for 0% (black curves in Figure 3c) and -0.86% (red curves in Figure 3c) strain condition. By carefully studying the rise/fall edges of the response time curves, a second-order exponential function was employed for fitting^[25,26] to calculate the rise and fall times (see Figure S3a–d, Supporting Information). Upon straining (-0.86%), the UV detection rise time decreases from 0.63 s (Figure S3a) to 0.61 s (Figure S3c); the fall time decreases from 4.88 s (Figure S3b) to 1.26 s (Figure S3d). The shortened response time results from strain-induced piezo-polarization charges present in the vicinity of the CdS/ZnO heterojunctions, which effectively reduce the barrier height (Figure 2f); this facilitates the separation and transport process of photogenerated carriers, and thus shortens the response time at rise/fall

edges. The visible response was derived under 532 nm off-axial illumination at an intensity of $1.5 \times 10^{-3} \text{ W cm}^{-2}$ (Figure 3f). The corresponding rise and fall times are calculated to be 25 ms (Figure S3e) and 452 ms (Figure S3f), using the same exponential fitting function as above. The best response time was observed under 325 nm off-axial illumination at an intensity of $5.9 \times 10^{-5} \text{ W cm}^{-2}$ as shown in the inset of Figure 3c, with a rise time of 20 ms and a fall time of 43 ms. These performances are impressive and competitive with other reported nanostructure-based UV detectors.^[25,27,28]

A piezo-phototronic effect was then applied to enhance/optimize the performance of OF–NW hybridized PDs for UV detection. A series of strains (from 0% to -0.86%) were externally applied to the device under axial illumination with a 325 nm laser for various power densities. The optoelectronic behavior was then monitored; the results shown in Figure 4a and Figure S4 in the Supporting Information signify an obvious enhancement in the photoresponse with an output current that increases linearly if more strain is applied to the PDs. This linear relationship between the current and the strain provides a potential application for real-time dynamic strain monitoring (see Supporting Information). To demonstrate the mechanism of current increases more clearly, the relative difference between the photocurrent and dark current for a certain power

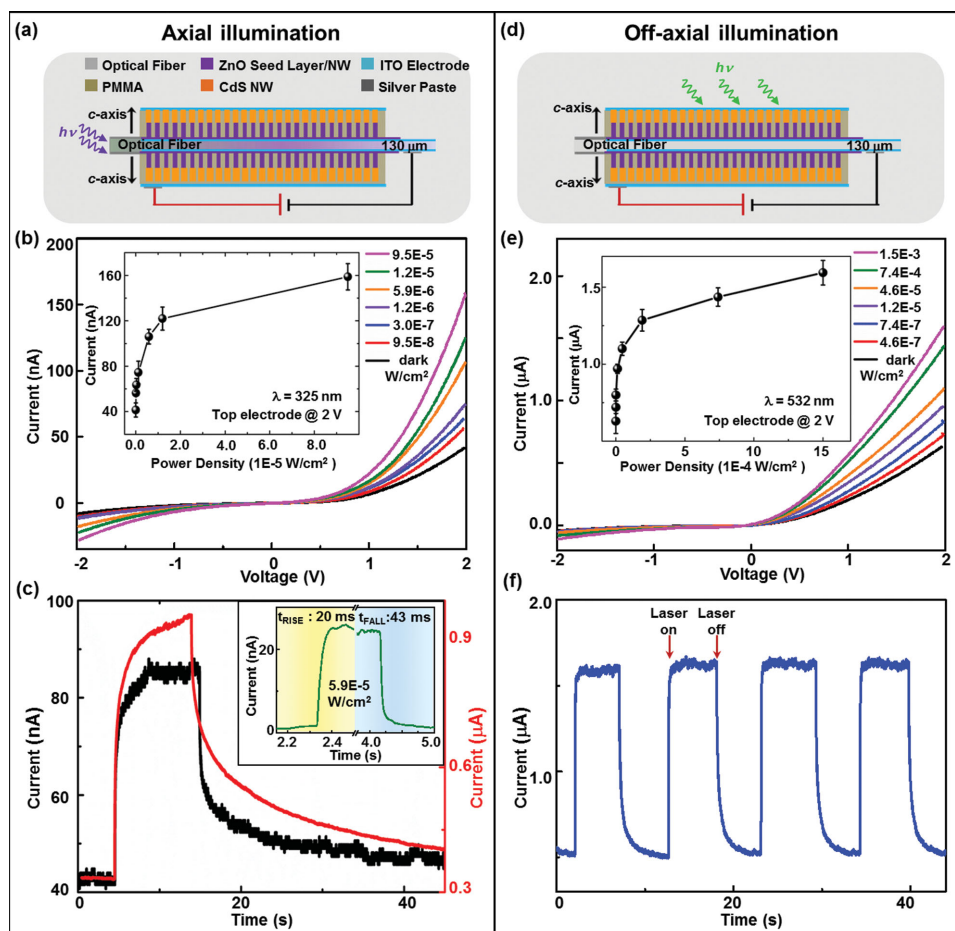


Figure 3. Demonstration of UV/visible detections of OF–NW hybridized PDs. UV detection (left panel): a) Schematic illustration, b) I – V characteristics, and c) response time of an OF–NW hybridized PD under 325 nm axial illuminations. The inset of (b) shows the current change with power density when the top electrode is biased at 2 V. The inset of (c) shows the response time of a PD under 325 nm off-axis illumination at a power density of $1.5 \times 10^{-5} \text{ W cm}^{-2}$. Visible detection (right panel): d) Schematic illustration, e) I – V characteristics, and f) time response of an OF–NW hybridized PD under 532 nm off-axis illumination. The inset of (e) shows the current change with varying power densities when the top electrode is biased at 2 V.

density value and strain condition with respect to the corresponding dark current is defined as $\Delta I / I_{\text{dark},s} = \frac{I_{\text{light},s} - I_{\text{dark},s}}{I_{\text{dark},s}}$,

where $I_{\text{light},s}$ and $I_{\text{dark},s}$ are the output current with and without illumination under a certain external strain (indicated by subscript “s”), respectively. The photosensitivity of the OF–NW hybridized UV PD for different power densities and strains was derived and the results have been summarized in Figure 4b. Generally, a better sensitivity is achieved when higher strains are applied. A local maximum is observed under strong light illumination (pink, green, and orange lines in Figure 4b), while the sensitivity fades away when the power density is reduced (blue, red and black lines in Figure 4b). These phenomena are attributed to the screening effect against piezo-polarization charges induced by light-generated free charge carriers.^[19] Under strong illumination, a huge amount of free carriers is generated to partially screen the piezo-polarization charges present in the vicinity of the ZnO/CdS heterojunction interface, forming a competing mechanism and thus leading to a local maximum; under weak illumination, strain-induced piezo-charges are still in dominance without a local extreme obtained

in sensitivity. More detailed analysis of the local maximum is found in the Supporting Information.

Another critical parameter to evaluate the performance of the PDs is the photoresponsivity R , which was calculated and analyzed comprehensively. Figure 4c shows the photoresponsivity under various strain and power density conditions at a top-electrode bias voltage of 2 V. The photoresponsivity R is defined as $R = \frac{I_{\text{light},s} - I_{\text{dark},s}}{P_{\text{ill}}} = \frac{\eta_{\text{ext}} q}{h\nu} \cdot \Gamma_{\text{c}}$,^[29] where $P_{\text{ill}} = I_{\text{ill}} \times S$ is the illumination power on the PD, Γ_{c} is the internal gain, η_{ext} is the external quantum efficiency (EQE), which can be assumed as unity^[25,30] to obtain the internal gain for simplicity, q is the electronic charge, h is Planck’s constant, ν is the frequency of the light, I_{ill} is the excitation power density, and S is the effective area of the PDs. A monotonous increase of R with applied strain was observed (Figure 4c) for each power density, with the largest R value reaching $1.2 \times 10^4 \text{ A W}^{-1}$ when applying a -0.86% strain on the PD under 325 nm laser axial illumination with a power density of $3.0 \times 10^{-7} \text{ W cm}^{-2}$. By assuming EQE equals 1, the internal gain of this PD is calculated as 4.58×10^4 , which can be induced by the heterojunction at the interface of

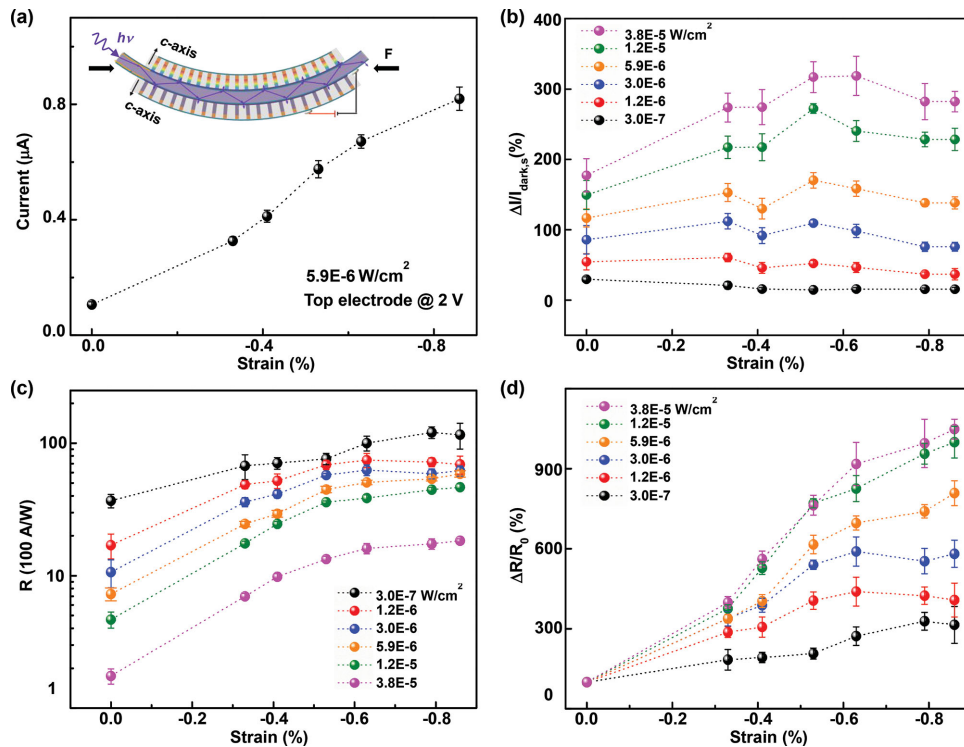


Figure 4. Piezo-phototronic effect on OF-NWs hybridized UV PDs under axial illuminations. a) I -strain curve of an OF-NWs hybridized UV PD under 325 nm axial illumination with a power density of $5.9 \times 10^{-6} \text{ W cm}^{-2}$ when the top electrode is biased at 2 V. The inset shows a corresponding schematic experiment set-up. b) Sensitivity, c) photoresponsivity R , and d) relative changes of R of an OF-NW hybridized UV PD operating in axial illumination mode under a series of power density and external strain conditions, for a top electrode bias voltage of 2 V. $I_{\text{dark},s}$ is the dark current under the corresponding external strain, ΔI is the photocurrent under a certain external strain. R_0 is the photoresponsivity under no strain. ΔR is the difference between photoresponsivity under strained and unstrained conditions.

the ZnO and CdS nanostructures and the presence of oxygen-related hole-trapping states at the NW surface.^[25] The achieved photoresponsivity R value is much larger than that of commercial UV PDs (mostly in the range of 0.1 – 0.2 A W^{-1}),^[31,32] and also near 10^5 times larger in magnitude than that obtained for a Si/ZnO core-shell NW array PD ($1.0 \times 10^{-2} \text{ A W}^{-1}$, 480 nm, -1 V),^[33] 10^3 times larger in magnitude than that of a Si/CdS core-shell NW network PD ($<1 \text{ A W}^{-1}$, 480 nm, -1 V).^[34] Lower photoresponsivity R observed at higher power density could be a consequence of saturation absorption of photons by the semiconductors, as reported previously in a ZnO-NW-based UV light PD.^[19] The difference between the photonic and dark current is not linearly proportional to the light intensity, and hence R decreases with increasing power density of the incident light.

A better insight into the piezo-phototronic effect on the photoresponsivity R can be derived by calculating the relative changes of R as $\Delta R/R_0$ (R_0 is the corresponding R under strain-free conditions) for each power density (Figure 4d). This value increases when either stronger incident light or larger external strain is applied (Figure 4d); the largest value obtained for $\Delta R/R_0$ was 1048% at the strongest power density ($3.8 \times 10^{-5} \text{ W cm}^{-2}$) and largest external strain (-0.86%) when the PD was operated under 325 nm laser axial illumination mode. The specific detectivity D^* ^[30] was also calculated, with the formula $D^* = R/(2eI_{\text{dark},s}/S)^{0.5}$, where $I_{\text{dark},s}$ is the dark current under the corresponding external strain (considered as the

major noise), S is the surface area of the PD. Figure S5 in the Supporting Information presents a monotonous increase of D^* for various applied external strain under each incident light power density. The highest detectivity of 1.1×10^{15} Jones was derived for a power density of $3.0 \times 10^{-7} \text{ W cm}^{-2}$.

UV detection under off-axial illumination was also investigated to provide a direct comparison with the axial mode. The results of the measurements are summarized in Figure S6 and S7 in the Supporting Information, showing a similar optoelectronic behavior as the axial illumination mode but with some distinguishable differences. The output current shown in Figure 4a and Figure S6a in the Supporting Information show a similar signal level, while the light stimuli applied under axial illumination (Figure 4a) is about 10% in power density of that employed for off-axial illumination (Figure S6a). These results indicate that OF-NW hybridized PDs under axial illumination show a response to much weaker incident light at the same output signal level in comparison to off-axial illumination, demonstrating a better sensitivity and responsivity under axial illumination. Furthermore, the photoresponsivity R reaches the highest value of 17.5 A W^{-1} ($9.5 \times 10^{-7} \text{ W cm}^{-2}$, -0.86% strain) under off-axial illumination (Figure S7c, Supporting Information). Compared with the highest value of R under axial illumination, $1.2 \times 10^4 \text{ A W}^{-1}$, a huge difference of three orders of magnitude was found here, as a consequence of the extended interaction length between the light and the NW array under axial illumination mode. Therefore, OF-NW hybridized PDs

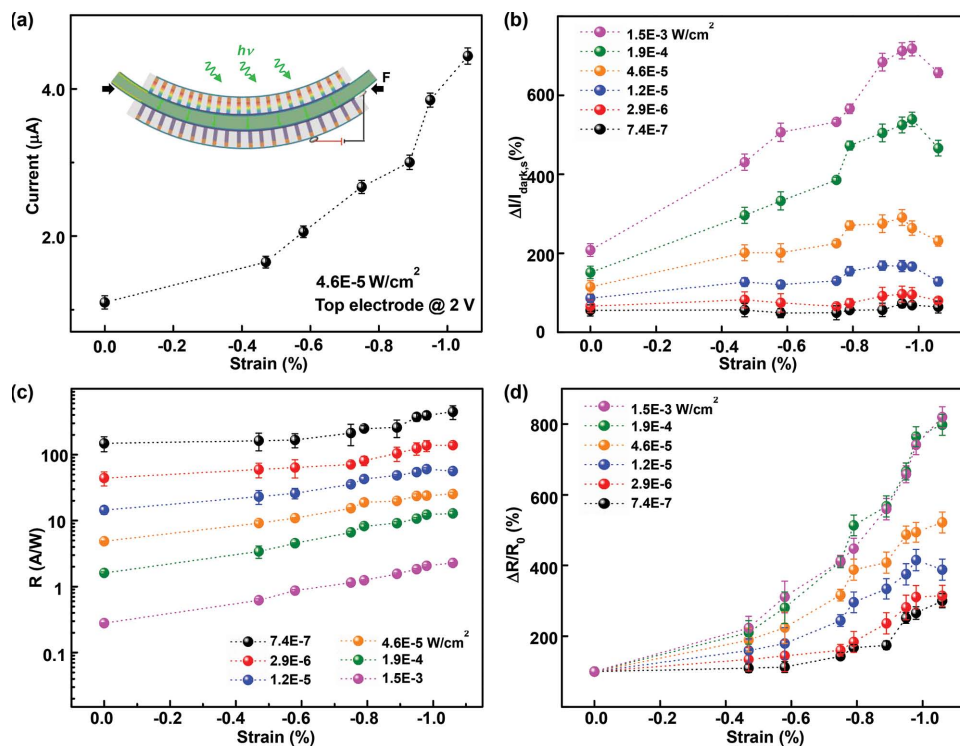


Figure 5. Piezo-phototronic effect on OF–NW hybridized visible PDs under off-axial illumination. a) I -strain curve of an OF–NW hybridized visible PD under 532 nm off-axial illuminations with a power density of $4.6 \times 10^{-5} \text{ W cm}^{-2}$ when the top electrode is biased at 2 V. The inset shows a corresponding schematic experiment set-up. b) Sensitivity, c) photoresponsivity R , and d) relative changes of R of an OF–NW hybridized visible PD operating in off-axial illumination mode under a series of power density and external strain conditions, for a top electrode bias voltage of 2 V. $I_{\text{dark},s}$ is the dark current under the corresponding external strain, ΔI is the photocurrent under a certain external strain. R_0 is photoresponsivity under no strain. ΔR is the difference between the photoresponsivity under strained and unstrained conditions.

under axial illumination display a superb performance compared to off-axial illumination for UV detection.

Piezo-phototronic-effect enhanced visible detection of our OF–NW hybridized PDs was also carefully studied in a similar manner under 532 nm off-axial illumination. I - V characteristics, sensitivity, photoresponsivity R and its relative changes were all systematically investigated; the results are summarized in Figures 5 and S8 (Supporting Information) for all power density and strain conditions, showing similar changes to those shown in Figure 4. Under 532 nm off-axial illuminations, the highest relative sensitivity achieved was 718% (Figure 5b) by applying a -0.98% strain on the PD at a power density of $1.5 \times 10^{-3} \text{ W cm}^{-2}$; the largest photoresponsivity R measured was 446 A W^{-1} (Figure 5c) at -1.06% strain and a power density of $7.4 \times 10^{-7} \text{ W cm}^{-2}$; the largest relative change of R of 820% (Figure 5d) was obtained at -1.06% strain and $1.5 \times 10^{-3} \text{ W cm}^{-2}$ power density. These results demonstrate the capabilities of our OF–NW hybridized PDs for visible detection. Visible detection under axial illumination was also studied and the results are presented in Figure S9 in the Supporting Information, but it proved to be a poor detector. More discussion is found in the Supporting Information.

The stability and reproducibility of our OF–NW hybridized PDs were also investigated and the results have been summarized in Figures S10 and S11 (Supporting Information) by providing more statistics of our measurements. During our experiments, over 100 devices were carefully studied. Figure S10 in

the Supporting Information presents the measured results of one typical PD operating under 325 nm axial illumination for four strains (0, -0.41% , -0.63% , -0.86%) and light intensities (3×10^{-7} , 3×10^{-6} , 1.2×10^{-5} , $3.8 \times 10^{-5} \text{ W cm}^{-2}$), indicating that our devices showed high stability and reproducibility. Figure S11 in the Supporting Information shows the repeatedly measured results of four strain-free PDs under 325 nm axial illumination at an intensity of $3.0 \times 10^{-7} \text{ W cm}^{-2}$, each for ten cycles.

Our OF–NW hybridized UV/visible PDs possess novel designed configurations mainly in two aspects. First, the optical fiber is employed as the foundation of this PD, which enables two working modes, i.e., axial illumination with light propagating inside the OF due to its light-guiding features and internal multi-reflection, and off-axial illumination with incident light applied on its surface to interact with most NWs through transmitting and scattering of light by the transparent OF core. Direct integration with an optical communication system can also be achieved by utilizing fiber welding technology in a coupler-free manner. Second, the newly designed engineering method and OF–NW hybridized concept demonstrated in this work can be extended to combinations of other materials,^[35–39] including infrared-sensitive materials and piezoelectric materials, and thus broaden the spectra ranges for more practical applications. Based on these newly designed OF–NW hybridized PDs, we achieved a response time as fast as 20 ms and R as high as $1.2 \times 10^4 \text{ A W}^{-1}$, both of which are competitive and

impressive compared with other reported nanostructure-based PDs.^[15,40] The introduction of the three-way coupling piezo-phototronic effect provides a feasible approach to enhance/optimize the performance of these PDs. Utilizing positive piezopolarization charges induced in the vicinity of the ZnO/CdS heterojunction interface upon straining to effectively modulate the barrier height formed at the local interface, piezo-phototronic effect successfully tune/control the electronic transport and optoelectronic processes, when charge carriers travel across the heterojunction interface. An enhancement/optimization in PD sensitivity of up to 718% (−0.98% strain, $1.5 \times 10^{-3} \text{ W cm}^{-2}$ at 532 nm off-axial illumination) and photoresponsivity of up to 2067% (−0.86% strain, $9.5 \times 10^{-4} \text{ W cm}^{-2}$ at 325 nm off-axial illumination) can be achieved by applying external strain. Possible applications of this newly designed piezo-phototronic PD may include energy-efficient optical communication systems, detection of weak signals and in formerly unreachable areas, safety monitoring of optical communication systems, damage-free mapping of the electromagnetic field distribution in isolated systems, and bio-compatible optoelectronic probes.

Experimental Section

Photodetector Fabrication Process: In our experiments, the ethylene tetrafluoroethylene (ETFE) jacket of the optical fibers provided by OFS Optics (HCS 200) was mechanically stripped and the polymer cladding (only remaining at one end of the OF) was removed with acetone. Then, the fibers were ultrasonically cleaned for 5 min consecutively in acetone, distilled water, and ethanol. Next, a layer of 100 nm ITO bottom-electrode followed by another 100 nm ZnO seed layer were deposited on the optical fibers by radio-frequency (RF) magnetron sputtering at room temperature (PVD75 system, Kurt. J. Lesker Company). The ITO layer serves not only as a conductive electrode, but also as a high-refractive-index material that allows light to escape from the fiber to interact with ZnO NWs. The coated OFs are then placed into mixed nutrient solutions (0.02 mM $\text{Zn}(\text{NO}_3)_2$ and 0.02 mM HMTA) for ZnO NW growth via a hydrothermal method in a mechanical convection oven (model Yamato DKN400, Santa Clara, CA, USA) at 85 °C for 3 h. In order to separate the ZnO NWs, 0–5 mL ammonium hydroxide (Sigma–Aldrich) was added per 100 mL mixing solution. The CdS layer was synthesized on top of the ZnO NWs by transferring the OFs of the last step into a Teflon-lined stainless autoclave, which contained the nutrition solution, as described in one of our previous publications;^[11] the autoclave was sealed and maintained at 200 °C for 12 h. After cooling the entire system, the product was washed with ethanol and distilled water, and then collected and vacuum-dried. A thin layer of PMMA was applied to enclose the main body of the NW array for insulation but leaving the fresh and clean CdS NW tips exposed by way of oxygen plasma etching. Another thin layer of ITO (100 nm) was deposited afterward to serve as the transparent top-electrode. Testing wires were connected to the top and bottom electrodes by silver paste, which could also attach the two ends of the OF–NW hybridized PD on a PET/PS substrate (with a typical length of 5 cm, width of 2 cm, and thickness of 0.5 mm). Finally, a thin layer of PDMS was employed to package the device to improve its mechanical robustness and resistance to environmental contamination and corrosion.

Materials Characterization: Detailed microscopic structures of ZnO and CdS NWs were characterized by scanning electron microscopy (SEM) (Hitachi SU8010), transmission electron microscopy (TEM) (Tecnaï G2) with selected area electron diffraction (SAED), and HRTEM (FEI F30) with energy-dispersive X-ray spectroscopy (EDX).

Measurements: *I*–*V* characteristics of the device were measured and recorded by a computer-controlled measurement system with a Stanford SRS Low noise current preamplifier (SR570)/SRS Low noise voltage

preamplifier (SR560) in conjunction with a GPIB controller (GPIB-USB-HS, NI 488.2). The optical input stimuli were provided by a He–Cd laser (wavelength = 325 nm, Model No. K157511-G, Kimmon Koha Co., Ltd.) and a green laser pointer (wavelength = 532 nm). A continuously variable filter was used to control the light power density, which was measured by a thermopile powermeter (Newport 818P-001-12). A high UV focusing objective was used to focus 325 nm UV laser into optical fiber under axial illumination mode measurements.

Power Density of Incident Light: The coupling efficiency between the laser beam and OF is greatly affected by the treatment technology applied to the fiber end face. In our experiments, we used an optical fiber clamp for simple handling of the end face of the optical fiber core. In order to estimate the coupling efficiency between the optical fiber and the incident light, we measured the output light intensity at one end of the optical fiber by applying an incident laser beam with known intensity from the other end, as schematically shown in Figure S12 in the Supporting Information. A coupling efficiency of about 10% was derived from this experiment. The photoresponsivity in Figure 4c and the relative photoresponsivity in Figure 4d corresponding to axial illumination mode were calculated based on this result.

Supporting Information

Supporting Information is available from the Wiley Online Library or from the author.

Acknowledgements

Z.N.W. and R.M.Y. contributed equally to this work. This research was supported by BES DOE (DE-FG02-07ER46394), MANA, National Institute For Materials Science, Japan, the Hightower Chair foundation, the “Thousand Talents” program for a pioneer researcher and his innovation team, and NNSF (Nos. 11104016), China.

Received: November 18, 2014

Revised: December 3, 2014

Published online:

- [1] K. T. V. Grattan, T. Sun, *Sens. Actuators, A* **2000**, *82*, 40.
- [2] I. Hartl, X. D. Li, C. Chudoba, R. K. Ghanta, T. H. Ko, J. G. Fujimoto, J. K. Ranka, R. S. Windeler, *Opt. Lett.* **2001**, *26*, 608.
- [3] J. Gowar, *Optical Communication Systems (2nd ed.)*, Prentice-Hall, Inc., Upper Saddle River, NJ, USA **1993**.
- [4] M. Iida, K. Hagiwara, H. Asakura, *Appl. Opt.* **1992**, *31*, 3015.
- [5] M. Binda, D. Natali, A. Iacchetti, M. Sampietro, *Adv. Mater.* **2013**, *25*, 4335.
- [6] M. H. Huang, S. Mao, H. Feick, H. Q. Yan, Y. Y. Wu, H. Kind, E. Weber, R. Russo, P. D. Yang, *Science* **2001**, *292*, 1897.
- [7] W. Z. Wu, X. N. Wen, Z. L. Wang, *Science* **2013**, *340*, 952.
- [8] C. F. Pan, L. Dong, G. Zhu, S. M. Niu, R. M. Yu, Q. Yang, Y. Liu, Z. L. Wang, *Nat. Photonics* **2013**, *7*, 752.
- [9] H. Yan, H. S. Choe, S. W. Nam, Y. J. Hu, S. Das, J. F. Klemic, J. C. Ellenbogen, C. M. Lieber, *Nature* **2011**, *470*, 240.
- [10] C. Y. Hsu, D. H. Lien, S. Y. Lu, C. Y. Chen, C. F. Kang, Y. L. Chueh, W. K. Hsu, J. H. He, *ACS Nano* **2012**, *6*, 6687.
- [11] F. Zhang, S. M. Niu, W. X. Guo, G. Zhu, Y. Liu, X. L. Zhang, Z. L. Wang, *ACS Nano* **2013**, *7*, 4537.
- [12] K. Heo, H. Lee, Y. Park, J. Park, H. J. Lim, D. Yoon, C. Lee, M. Kim, H. Cheong, J. Park, J. Jian, S. Hong, *J. Mater. Chem.* **2012**, *22*, 2173.
- [13] S. Bai, W. W. Wu, Y. Qin, N. Y. Cui, D. J. Bayerl, X. D. Wang, *Adv. Funct. Mater.* **2011**, *21*, 4464.
- [14] C. Y. Lu, S. J. Chang, S. P. Chang, C. T. Lee, C. F. Kuo, H. M. Chang, Y. Z. Chiou, C. L. Hsu, I. C. Chen, *Appl. Phys. Lett.* **2006**, *89*, 153101.

- [15] M. W. Chen, J. R. D. Retamal, C. Y. Chen, J. H. He, *IEEE Electron Device Lett.* **2012**, *33*, 411.
- [16] D. S. Tsai, W. C. Lien, D. H. Lien, K. M. Chen, M. L. Tsai, D. G. Senesky, Y. C. Yu, A. P. Pisano, J. H. He, *Sci. Rep.* **2013**, *3*, 2628.
- [17] J. R. D. Retamal, C. Y. Chen, D. H. Lien, M. R. S. Huang, C. A. Lin, C. P. Liu, J. H. He, *ACS Photonics* **2014**, *1*, 354.
- [18] Z. L. Wang, *Adv. Mater.* **2012**, *24*, 4632.
- [19] Q. Yang, X. Guo, W. H. Wang, Y. Zhang, S. Xu, D. H. Lien, Z. L. Wang, *ACS Nano* **2010**, *4*, 6285.
- [20] Q. Yang, Y. Liu, C. F. Pan, J. Chen, X. N. Wen, Z. L. Wang, *Nano Lett.* **2013**, *13*, 607.
- [21] Y. F. Hu, Y. Zhang, C. Xu, L. Lin, R. L. Snyder, Z. L. Wang, *Nano Lett.* **2011**, *11*, 2572.
- [22] R. M. Yu, L. Dong, C. F. Pan, S. M. Niu, H. F. Liu, W. Liu, S. Chua, D. Z. Chi, Z. L. Wang, *Adv. Mater.* **2012**, *24*, 3532.
- [23] R. S. Yang, Y. Qin, L. M. Dai, Z. L. Wang, *Nat. Nanotechnol.* **2009**, *4*, 34.
- [24] Y. Xu, M. A. A. Schoonen, *Am. Mineral.* **2000**, *85*, 543.
- [25] C. Soci, A. Zhang, B. Xiang, S. A. Dayeh, D. P. R. Aplin, J. Park, X. Y. Bao, Y. H. Lo, D. Wang, *Nano Lett.* **2007**, *7*, 1003.
- [26] P. N. Ni, C. X. Shan, S. P. Wang, X. Y. Liu, D. Z. Shen, *J. Mater. Chem. C* **2013**, *1*, 4445.
- [27] H. K. Yadav, K. Sreenivas, V. Gupta, *Appl. Phys. Lett.* **2010**, *96*, 223507.
- [28] J. Zhou, Y. Gu, Y. Hu, W. Mai, P. H. Yeh, G. Bao, A. K. Sood, D. L. Polla, Z. L. Wang, *Appl. Phys. Lett.* **2009**, *94*, 191103.
- [29] G. Konstantatos, E. H. Sargent, *Nat. Nanotechnol.* **2010**, *5*, 391.
- [30] X. Liu, L. L. Gu, Q. P. Zhang, J. Y. Wu, Y. Z. Long, Z. Y. Fan, *Nat. Commun.* **2014**, *5*, 4007.
- [31] E. Monroy, F. Omnes, F. Calle, *Semicond. Sci. Technol.* **2003**, *18*, R33.
- [32] J. P. Zou, Q. Zhang, K. Huang, N. Marzari, *J. Phys. Chem. C* **2010**, *114*, 10725.
- [33] K. Sun, Y. Jing, N. Park, C. Li, Y. Bando, D. L. Wang, *J. Am. Chem. Soc.* **2010**, *132*, 15465.
- [34] S. Manna, S. Das, S. P. Mondal, R. Singha, S. K. Ray, *J. Phys. Chem. C* **2012**, *116*, 7126.
- [35] G. Konstantatos, I. Howard, A. Fischer, S. Hoogland, J. Clifford, E. Klem, L. Levina, E. H. Sargent, *Nature* **2006**, *442*, 180.
- [36] E. H. Sargent, *Adv. Mater.* **2008**, *20*, 3958.
- [37] S. A. McDonald, G. Konstantatos, S. G. Zhang, P. W. Cyr, E. J. D. Klem, L. Levina, E. H. Sargent, *Nat. Mater.* **2005**, *4*, 138.
- [38] G. Sarasqueta, K. R. Choudhury, F. So, *Chem. Mater.* **2010**, *22*, 3496.
- [39] G. Sarasqueta, K. R. Choudhury, J. Subbiah, F. So, *Adv. Funct. Mater.* **2011**, *21*, 167.
- [40] C. Liu, B. P. Zhang, Z. W. Lu, N. T. Binh, K. Wakatsuki, Y. Segawa, R. Mu, *J. Mater. Sci.: Mater. Electron.* **2009**, *20*, 197.